

# Energy-resolved detection of precipitating electrons of 30-100 keV by a sounding rocket associated with dayside chorus waves

Sugo Shin<sup>1</sup>, Kawashima Oya<sup>1</sup>, Kasahara Satoshi<sup>1</sup>, Asamura Kazushi<sup>2</sup>, Nomura Reiko<sup>3</sup>, Miyoshi Yoshizumi<sup>4</sup>, Ogawa Yasunobu<sup>5</sup>, Hosokawa Keisuke<sup>6</sup>, Mitani Takefumi<sup>7</sup>, Namekawa Taku<sup>8</sup>, Sakanoi Takeshi<sup>9</sup>, Fukizawa Mizuki<sup>9</sup>, Yagi Naoshi<sup>9</sup>, Fedorenko Yury V.<sup>10</sup>, Nikitenko Alexander<sup>10</sup>, Yokota Shoichiro<sup>11</sup>, Keika Kunihiro<sup>1</sup>, Hori Tomoaki<sup>4</sup>, and Koehler Christopher<sup>12</sup>

<sup>1</sup>The University of Tokyo

<sup>2</sup>The Institute of Space and Astronautical Science

<sup>3</sup>Tsukuba Space Center, Japan Aerospace Exploration Agency

<sup>4</sup>Institute for Space-Earth Environmental Research, Nagoya University

<sup>5</sup>National Institute of Polar Research

<sup>6</sup>University of Electro-Communications

<sup>7</sup>ISAS/JAXA

<sup>8</sup>University of Tokyo

<sup>9</sup>Tohoku University

<sup>10</sup>Polar Geophysical Institute

<sup>11</sup>Osaka University

<sup>12</sup>University of Colorado Boulder

November 16, 2022

## Abstract

Whistler mode chorus waves scatter magnetospheric electrons and cause precipitation into the Earth's atmosphere. Previous measurements showed that nightside chorus waves are indeed responsible for diffuse/pulsating aurora. Although chorus waves and electron precipitation have also been detected on the dayside, their link has not been illustrated (or demonstrated) in detail compared to the nightside observations. Conventional low-altitude satellite observations do not well resolve the energy range of 10–100 keV, hampering verification on resonance condition with chorus waves. In this paper we report observations of energetic electrons with energies of 30–100 keV that were made by the electron sensor installed on the NASA's sounding rocket RockSat-XN. It was launched from the Andøya Space Center on the dayside (MLT  $\sim$  11 h) at the L-value of  $\sim$  7 on 13 January 2019. Transient electron precipitation was observed at  $\sim$  50 keV with the duration of  $<$ 100 s. A ground station at Kola peninsula in Russia near the rocket's footprint observed intermittent emissions of whistler-mode waves simultaneously with the rocket observations. The energy of precipitating electrons is consistent with those derived from the quasi-linear theory of pitch angle scattering by chorus waves through cyclotron resonance, assuming a typical dayside magnetospheric electron density. Precise interaction region is discussed based on the obtained energy spectrum below 100 keV.

1 Energy-resolved detection of precipitating electrons of 30–  
2 100 keV by a sounding rocket associated with dayside chorus  
3 waves

4 S. Sugo<sup>1</sup>, O. Kawashima<sup>1</sup>, S. Kasahara<sup>1</sup>, K. Asamura<sup>2</sup>, R. Nomura<sup>3</sup>, Y. Miyoshi<sup>4</sup>, Y.  
5 Ogawa<sup>5</sup>, K. Hosokawa<sup>6</sup>, T. Mitani<sup>2</sup>, T. Namekawa<sup>1,2</sup>, T. Sakanoi<sup>7</sup>, M. Fukizawa<sup>7</sup>, N.  
6 Yagi<sup>7</sup>, Y. Fedorenko<sup>8</sup>, A. Nikitenko<sup>8</sup>, S. Yokota<sup>9</sup>, K. Keika<sup>1</sup>, T. Hori<sup>4</sup>, C. Koehler<sup>10</sup>

7 <sup>1</sup>The University of Tokyo, Tokyo, Japan, <sup>2</sup>Japan Aerospace Exploration Agency,  
8 Kanagawa, Japan, <sup>3</sup>National Astronomical Observatory of Japan, Tokyo, Japan,  
9 <sup>4</sup>Nagoya University, Aichi, Japan, <sup>5</sup>National Institute of Polar Research, Tokyo, Japan,  
10 <sup>6</sup>The University of Electro-Communications, Tokyo, Japan, <sup>7</sup>Tohoku University,  
11 Miyagi, Japan, <sup>8</sup>Polar Geophysical Institute, Russia, <sup>9</sup>Osaka University, Toyonaka,  
12 Japan, <sup>10</sup>University of Colorado at Boulder, USA

13 **Key Points:**

- 14 • The relation between energetic electron precipitation and chorus waves at the dayside  
15 magnetosphere have not been identified in detail  
16 • Our sounding rocket experiment identified precipitating energetic electrons within  
17 typical resonance energy with chorus waves on the dayside  
18 • Ground-based and satellite observations of chorus waves support that the observed  
19 electron precipitation was caused by chorus waves

## 20 Abstract

21 Whistler mode chorus waves scatter magnetospheric electrons and cause precipitation into  
22 the Earth's atmosphere. Previous measurements showed that nightside chorus waves are  
23 indeed responsible for diffuse/pulsating aurora. Although chorus waves and electron  
24 precipitation have also been detected on the dayside, their link has not been illustrated (or  
25 demonstrated) in detail compared to the nightside observations. Conventional low-altitude  
26 satellite observations do not well resolve the energy range of 10–100 keV, hampering  
27 verification on resonance condition with chorus waves. In this paper we report observations  
28 of energetic electrons with energies of 30–100 keV that were made by the electron sensor  
29 installed on the NASA's sounding rocket RockSat-XN. It was launched from the Andøya  
30 Space Center on the dayside (MLT ~ 11 h) at the L-value of ~ 7 on 13 January 2019.  
31 Transient electron precipitation was observed at ~ 50 keV with the duration of <100 s. A  
32 ground station at Kola peninsula in Russia near the rocket's footprint observed intermittent  
33 emissions of whistler-mode waves simultaneously with the rocket observations. The energy  
34 of precipitating electrons is consistent with those derived from the quasi-linear theory of pitch  
35 angle scattering by chorus waves through cyclotron resonance, assuming a typical dayside  
36 magnetospheric electron density. Precise interaction region is discussed based on the obtained  
37 energy spectrum below 100 keV.

38

## 39 Plain Language Summary

40 The Earth's magnetosphere was filled with energetic electrons and various waves. Energetic  
41 electrons sometimes precipitate into the Earth's atmosphere and cause aurora. Whistler mode  
42 waves are believed to cause such precipitation and previous measurements showed that  
43 nightside chorus waves are responsible for aurora. Energetic electrons and chorus waves are  
44 also observed on the dayside magnetosphere. However, their link has not been illustrated in  
45 detail compared to the nightside observations. In this paper, we verified the energy spectrum  
46 of precipitating electrons on the dayside by installing the sensor which can resolve the 30–  
47 100 keV energy range on a sounding rocket and observed transient electron precipitation.

48

## 49 1 Introduction

50 Precipitating electrons from the magnetosphere have been measured by balloons, sounding  
51 rockets, and low-altitude satellites to investigate auroral zone phenomenology [e.g.,  
52 *Winningham et al.*, 1985; *Fuller-Rowell and Evans*, 1987; *Miyoshi et al.*, 2010, 2015a],  
53 radiation belt dynamics [e.g. *Millan and Thorne*, 2007; *Miyoshi et al.*, 2008] and effects on  
54 the chemical composition of the upper atmosphere [e.g., *Thorne et al.*, 1977; *Lam et al.*,  
55 2010; *Miyoshi et al.*, 2015b; *Turunen et al.*, 2016]. *Hardy et al.* [2008] conducted statistical  
56 studies based on the large database of energy spectra in the 50 eV–20 keV energy range  
57 accumulated by the Defense Meteorological Satellite Program (DMSP) and reported the  
58 distributions of electron precipitation depend on geomagnetic latitude (MLAT), magnetic  
59 local time (MLT) and Kp index.

60 *Millan and Thorne* [2007] reviewed observations of higher energy (~10s keV to ~MeV)  
61 electron precipitation as one of the radiation belt electron loss mechanisms. Quasi-periodic  
62 bursts of high-energy electron precipitation with short timescale (< 1s), called microbursts,  
63 were detected in balloon experiments and the SAMPEX satellite observations [e.g. *Anderson*  
64 *and Milton*, 1964; *Parks*, 1978; *Blake et al.*, 1996]. Statistical surveys from NOAA Polar  
65 Orbiting Environmental Satellites (POES) presented the global model of the energy-

66 integrated flux ( $> 30$  keV) of precipitating electrons as a function of geomagnetic activity  
67 [Lam *et al.*, 2010].

68 Whistler mode chorus waves are believed to play an important role in these electron  
69 precipitations. Chorus waves are electromagnetic emissions often composed of discrete rising  
70 or falling elements [e.g. Burtis and Helliwell, 1969; Sazhin and Hayakawa, 1992; Santlic *et*  
71 *al.*, 2003]. The typical frequency of chorus waves is  $0.1-0.8 f_{ce}$ , where  $f_{ce}$  is the equatorial  
72 electron cyclotron frequency, and has a frequency gap at  $\sim 0.5 f_{ce}$  [e.g. Burtis and Helliwell,  
73 1969; Tsurutani and Smith, 1974; Sazhin and Hayakawa, 1992]. Chorus waves are mostly  
74 observed on the nightside during disturbed geomagnetic conditions and confined near the  
75 magnetic equator [e.g. Tsurutani and Smith, 1977; Meredith *et al.*, 2012]. Meredith *et al.*  
76 [2012] showed that lower band chorus ( $0.1-0.5 f_{ce}$ ) is confined to less than  $15^\circ$  in MLAT on  
77 the night side and upper band chorus ( $0.5-0.8 f_{ce}$ ) is within about  $6^\circ$  in MLAT due to strong  
78 Landau damping. Chorus waves are responsible for energetic electron precipitation into the  
79 atmosphere by pitch angle scattering. On the nightside, recent evidence suggests that chorus  
80 waves are the dominant cause of electron pitch-angle scattering and resulting  
81 diffuse/pulsating aurora [e.g. Ni *et al.*, 2008, 2011; Nishimura *et al.*, 2010; Thorne *et al.*,  
82 2010; Miyoshi *et al.*, 2015a; Kasahara *et al.*, 2018a; 2019; Ozaki *et al.*, 2019; Hosokawa *et*  
83 *al.*, 2020; Nishimura *et al.*, 2020].

84 Dayside chorus waves are less dependent on the geomagnetic conditions and were observed  
85 over wider range of magnetic latitude than nightside chorus waves [Tsurutani and Smith,  
86 1977; Meredith *et al.*, 2012]. Meredith *et al.* [2012] showed that lower band chorus waves  
87 were observed up to  $30^\circ$  in MLAT on the dayside. These features derive from the distortion  
88 of the dayside magnetic field due to solar wind compression. The distortion forms two  
89 minima of magnetic field strength (minimum B pockets) at high latitudes of both  
90 hemispheres. Chorus waves can be generated at these regions [Vaivads *et al.*, 2007; Tsurutani  
91 *et al.*, 2009]. The distortion also forms the region called Dayside Uniform Zone (DUZ),  
92 where the gradient of the magnetic field strength along the field ( $dB/ds$ ) is nearly zero within  
93 a large range of magnetic latitude. Such a field line exists in the transition region between the  
94 dipole-like field near the Earth and the compressed field with minimum B pockets. Dayside  
95 chorus waves near the DUZ region were observed at the ground during quiet geomagnetic  
96 conditions [Keika *et al.*, 2012].

97 Despite such differences, dayside chorus waves are also expected to contribute to energetic  
98 electron precipitation in probably the same physical mechanisms as on the nightside. Dayside  
99 diffuse aurora by low energy electron precipitation were reported [e.g. Newell *et al.*, 2009;  
100 Han *et al.*, 2015] and Nishimura *et al.* [2013] indicated that chorus waves are the dominant  
101 cause of dayside diffuse aurora. At high latitude ( $L > 6$ ),  $< 100$  keV electrons are expected to  
102 efficiently resonate with chorus waves at the magnetic equator and off-equatorial minimum-B  
103 pockets and precipitate into the atmosphere. While high energy electrons were observed on  
104 the dayside [e.g. Parks *et al.*, 1978; Lam *et al.*, 2010], few previous observations have  
105 identified  $< 100$  keV because of the lack of energy resolution. Previous researches indirectly  
106 obtained precipitated flux in the range of  $30-100$  keV by subtracting the integral flux of  $> 100$   
107 keV from that of  $> 30$  keV [Ni *et al.*, 2014; Li *et al.*, 2013, 2014a, 2014b]. However, different  
108 channels have different efficiencies for incoming electrons and different proton  
109 contaminations, which are difficult to correct due to a lack of reliable proton measurements  
110 [Yando *et al.*, 2011; Askainen and Mursula, 2013], making it difficult to obtain reliable  
111 electron energy spectra at  $30-100$  keV.

112 In this paper, we investigate the energy spectrum of precipitating electrons of  $30-100$  keV on  
113 the dayside in order to discuss resonance condition. The electron sensor was installed on the

114 NASA's sounding rocket RockSat-XN, which was launched on the dayside (MLT ~ 11 h) at  
115  $L \sim 7$  from the Andøya Space Center. The electron sensor detected precipitating electrons in  
116 the sunlit region, where little research has been done on the precipitating electrons of 30-100  
117 keV. Section 2 describes instrumentation and installation on the sounding rocket. Section 3  
118 provides solar wind, geomagnetic condition and magnetospheric configuration. In section 4,  
119 we discuss the resonance condition based on chorus wave frequency measured at a ground  
120 station near the rocket's footprint.

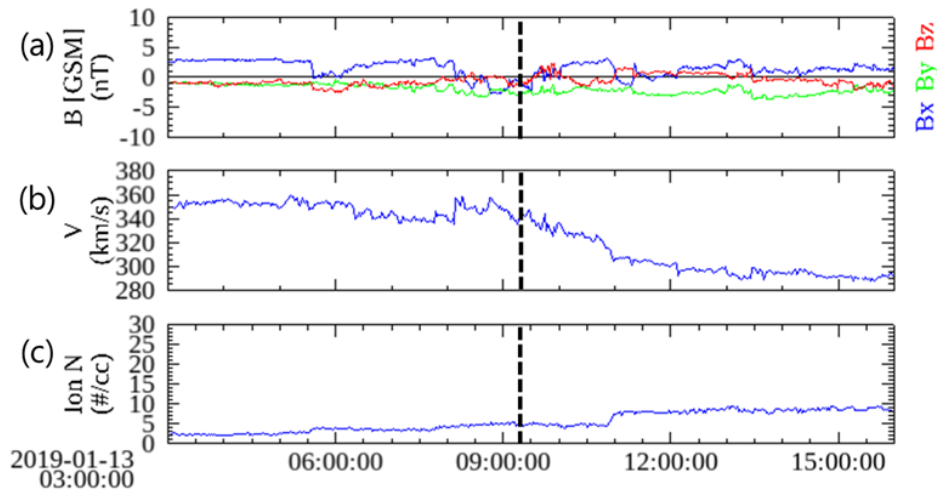
## 121 **2 Instrumentation**

122 Main results in this paper were obtained by Medium-energy Electron Detector (MED). MED  
123 can measure the electron velocity distribution functions in the energy range of 30–100 keV.  
124 MED is comprised of five pinholes and avalanche photodiodes (APD), covering nearly 2-pi  
125 steradian field of view. APDs provide higher signal-to-noise ratio than conventional solid-  
126 state detectors because of its internal gain and have advantage of high quantum efficiency for  
127 a few tens of keV electrons [Ogasawara *et al.*, 2005, 2006, 2008, 2016; Kasahara *et al.*,  
128 2010, 2012]. We utilized APDs with the thickness of  $\sim 70 \mu\text{m}$  to properly measure the  
129 incoming energy for 30–100 keV electrons. To attenuate protons and photons, APDs were  
130 covered by  $\sim 2 \mu\text{m}$  aluminum layer. Preamplifiers, shaping amplifiers, peak holders, and  
131 analog-to-digital converters are used to measure the incoming electron energy. Detected  
132 signals are binned into logarithmically separated sixteen pulse height channels depending on  
133 the incoming electron energy. A geometric factor of MED was  $7.7 \times 10^{-5} \text{ cm}^2 \text{ sr}$  per APD.  
134 Energy resolution was about 50% ( $< 10 \text{ keV}$ ) at half maximum for 20 keV electrons. Because  
135 higher energy electron is less dependent on attenuation by aluminum layer, energy resolution  
136 is higher for higher energy electron. For example, energy resolution was about 10% for 30  
137 keV and about 2% for 100 keV in Monte Carlo simulation.  
138 MED was installed on the sounding rocket in such a way that the angles between looking  
139 direction of five APDs and the rocket spin axis were  $30^\circ$ ,  $30^\circ$ ,  $90^\circ$ ,  $150^\circ$  and  $150^\circ$ . Fluxgate  
140 magnetometer was also mounted on the rocket. The RockSat-XN rocket was launched from  
141 Andøya Space Center in Norway at 0913 UT on 13 January 2019. The hemispherical field of  
142 view of MED covered most of the pitch angle range by the rocket spinning and coning,  
143 whose periods are  $\sim 1 \text{ s}$  and  $\sim 30 \text{ s}$ , respectively. We determined pitch angles by using the  
144 Fluxgate magnetometer, which was also onboard the rocket.

## 145 **3 Observation**

### 146 **3.1. Solar Wind and Geomagnetic Condition**

147 Figure 1 shows solar wind data from the WIND spacecraft between 0300 and 1600 UT on 13  
148 January 2019. A black dashed line indicates the launch time. Figure 1 (a) shows that  $Y_{\text{gsm}}$   
149 component of the interplanetary magnetic field was negative and  $Z_{\text{gsm}}$  component fluctuated  
150 within  $\pm 3 \text{ nT}$ . Figure 1 (b) and (c) show that the solar wind velocity was 340 km/s and ion  
151 density was  $5 \text{ cm}^{-3}$ , and the dynamic pressure was  $\sim 1 \text{ nPa}$ .

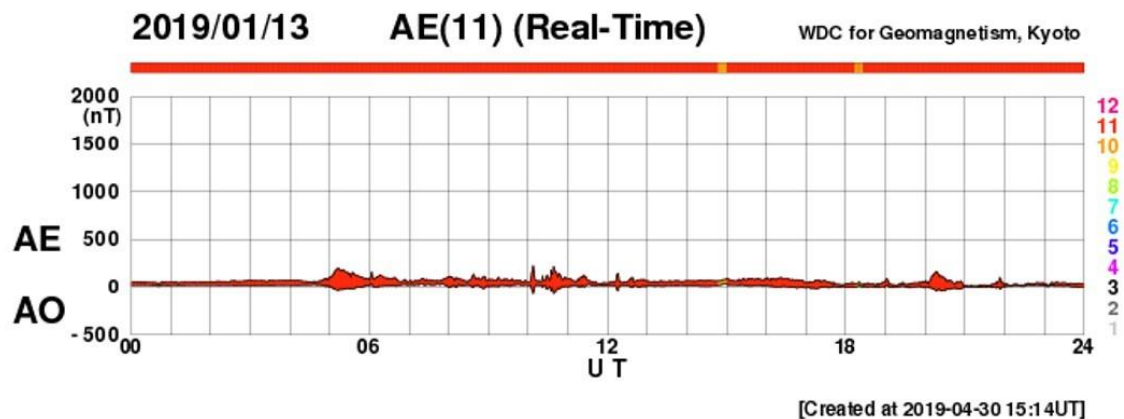


152  
 153 Figure 1. Time profile of the solar wind data from the WIND spacecraft between 0300 and  
 154 1600 UT on 13 January 2019. A black dashed line indicates the launch time of the RockSat-  
 155 XN rocket. (a) Three components of the interplanetary magnetic field in geocentric solar  
 156 magnetospheric coordinates. (b) Solar wind velocity data of the SWE instrument. (c) Ion  
 157 density obtained from the MFI, SWE and 3DP instruments.

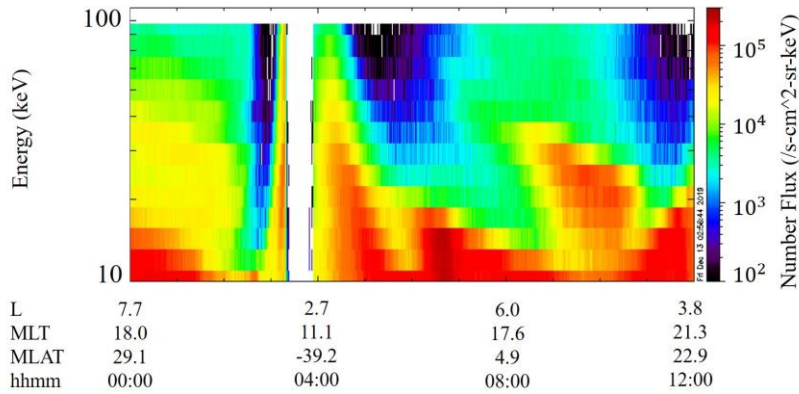
158  
 159 Figure 2 presents real-time AE index on 13 January 2019. The AE index was steady below  
 160 300 nT through the day of flight, but with small increase up to  $\sim 200$  nT around 0500 UT. The  
 161 3-hourly Kp index was in the range of 0 to 1 on 13 January 2019. These data suggest that the  
 162 period of flight was quiet in terms of solar wind and ground-based geomagnetic conditions.  
 163

### 164 3.2. Magnetospheric electrons

165 Figure 3 provides energy-time spectrogram of the spin-averaged electron energy flux from  
 166 MEP-e [Kasahara *et al.*, 2018a] onboard the ERG satellite [Miyoshi *et al.*, 2018a]. ERG  
 167 located at  $(X, Y, Z)_{\text{gsm}} = (-1, 6, 1) R_E$  and at the L-value of 6 around 0900 UT. The perigee  
 168 and the apogee are  $(X, Y, Z)_{\text{gsm}} = (-1, 0, 0) R_E$  around 1200 UT and  $(X, Y, Z)_{\text{gsm}} = (5, 2, 2)$   
 169  $R_E$  around 0800 UT respectively. In this figure, it can be seen that  $\sim 30$ -40 keV electron  
 170 energy flux increased at  $\sim 0800$  UT and lower energy electron flux also increased later. This  
 171 suggests that energetic electron injection into the magnetosphere occurred before 0800 UT.  
 172 This injection may be associated with the small increase of the AE index at  $\sim 0500$  UT.  
 173



174  
 175 Figure 2. One-day plot of the real-time AE and AO index on 13 January 2019. Color  
 176 represents the number of stations to derive the index. Color scale is displayed on the right  
 177 side of panel. There is small substorm event at  $\sim 0500$  UT.



178

179

180

181

182

Figure 3. Energy-time spectrogram of the spin-averaged electron energy flux from MEP-e onboard the ERG satellite on 13 January 2019. Enhancement of energetic electron flux was observed between 0800 and 1100 UT. L is the McIlwain L-shell derived from IGRF.

183

### 3.3. Rocket observations

184

185

186

187

188

189

190

191

192

193

194

195

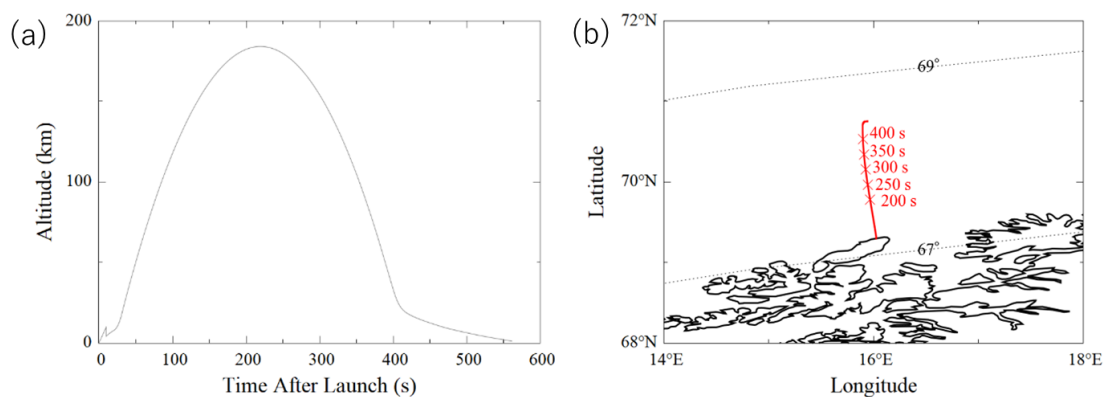
196

197

198

199

NASA's sounding rocket, RockSat-XN was launched at Andøya in Norway (69°17' N, 16°01' E) at 09:13 UT (10:13 LT) on 13 January 2019. Figure 4 shows that the altitude profile of this flight and the horizontal trajectory in the geographical coordinate. Figure 5 (a)–(e) present raw data energy spectra of pitch angles 0–90° (red) and 90–180° (blue) observed by MED for every 50 s from 120 s after the launch, where count rate is divided by the number of channels within 0–85° and 95–180° respectively. Pulse height channels are essentially proportional to the incoming energy. We do not discuss pulse height channels 0–2 because of the high noise level. As shown in Figures 5 (a), (b), (d), and (e), no significant difference between 0–85° and 95–180° spectra during most periods (120–220 s, 270–370 s after launch). This suggests that the detected signals were due to penetrating particles, whose incoming directions were not limited by the pinholes. We estimated count rates and energy deposit caused by penetrating galactic cosmic ray (GCR) proton. Count rates of GCR detected by APDs (size is 0.25 cm<sup>2</sup>) is estimated to be ~ 30 counts / 50 s, assuming typical GCR flux ~0.4 / cm<sup>2</sup>-s-sr in the solar minimum at the high latitude [Neher *et al.*, 1956], consistent with our observation. Energy deposit is ~30 keV, assuming that GCR with typical energy (~0.1–10 GeV) penetrating the 70 μm silicon APD, consistent with peak



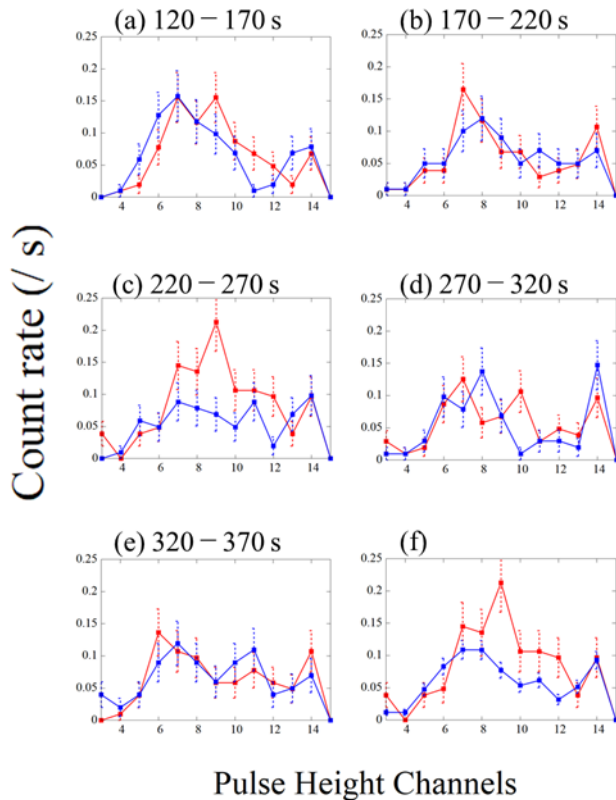
200

201

202

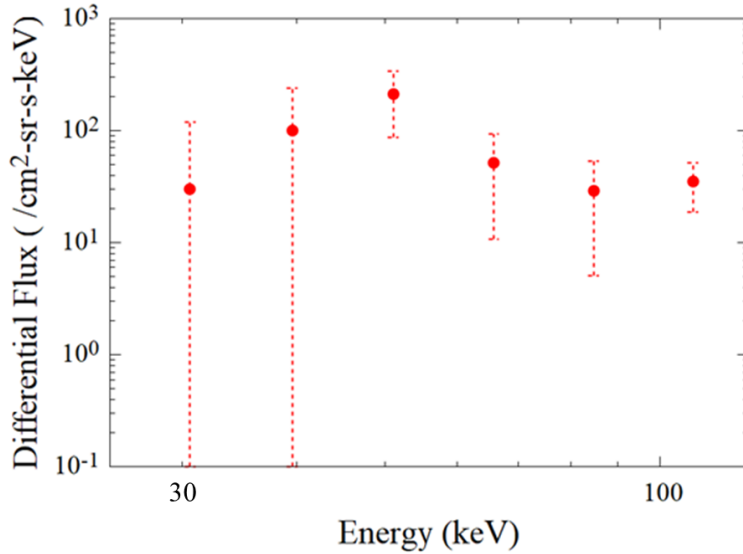
Figure 4. The rocket trajectory. (a) The altitude profile of the RockSat-XN rocket. (b) The position in the geographical coordinate (red line). Five cross marks shows the position 200, 250, 300, 350 and 400 s after launch. Black dotted lines represent geomagnetic latitude.

203 energy of energy spectra of pitch angle 0–85° and 95–180° (i.e., pulse height channel 7  
 204 corresponds to about 30 keV). Therefore, we conclude that most counts during 120–220 s and  
 205 270–370 s after the launch are due to GCR. Although upward-looking APDs may have  
 206 detected precipitating electrons as well, the precipitating electron flux level was too low to be  
 207 distinguished from GCR for most of the time.  
 208 Nevertheless, during 220–270 s after the launch (Figure 5c), counts of pitch angle 0–85° are  
 209 significantly higher than those of pitch angle 95–180° at pulse height channels 9–12. For this  
 210 time period, electrons of pitch angles 0–85° show a peak at the different energy from GCR’s  
 211 energy deposit, indicating the transient significant electron precipitation. In order to confirm  
 212 that two spectra are different, we conducted the Kolmogorov–Smirnov statistical test, which  
 213 examines null hypothesis that energy spectra of pitch angles 0–85° and 95–180° come from  
 214 the same population. The null hypothesis was rejected with significance level of ~0.4 %.  
 215 Furthermore, we assume that the spectrum of GCR was constant during the whole flight  
 216 period and averaged the energy spectra of pitch angle 0–85° for 120–370 s, so that the error  
 217 of the energy spectrum of GCR becomes less (Figure 5f, blue line). We performed the  
 218 Kolmogorov–Smirnov test again for the averaged spectrum of GCR and that of pitch angle 0–  
 219 85° during 220–370 s after launch as well and rejected the null hypothesis with significance  
 220 level of ~0.4%. No significant difference was found between spectra of pitch angle 0–85° and  
 221 GCR during the other periods. These data indicate that there was a transient electron  
 222 precipitation within ~100 s.



223  
 224  
 225  
 226  
 227  
 228  
 229  
 230

Figure 5. Energy spectra of pitch angles 0–85° (red) and 95–180° (blue) observed by MED during (a) 120–170 s, (b) 170–220 s, (c) 220–170 s, (d) 270–320 s, (e) 320–370 s, after the launch. Standard deviation assuming Poisson distribution counting statistics are shown by error bars. Pulse Height Channels are essentially proportional to the detected energy. The count rate is calculated by dividing the count detected by the five detectors facing the pitch angles of 0–85° or 95–180° by the observation time. (f) Energy spectrum of pitch angle 0–85° during 220–270 s (red) and that of pitch angle 95–180° for 120–370 s (blue).



231 Figure 6. Calibrated energy spectrum of precipitating electrons. Error bars indicate  $2\sigma$ , where  
 232  $\sigma$  is the standard error.

233

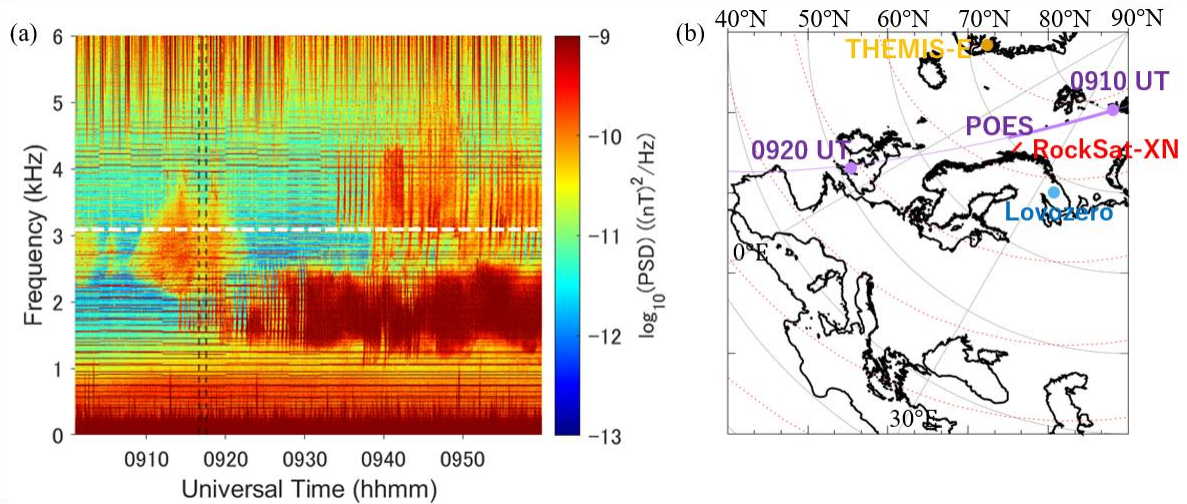
234 We calibrated pulse height channel to energy and counts to differential flux based on the  
 235 geometrical design and laboratory tests. Note that here we obtain the precipitating electron  
 236 counts by subtracting GCR contamination (Figure 5f, blue line) from the counts in the pitch  
 237 angle  $0-85^\circ$  during 220–270 s (Figure 5f, red line). Thus, obtained energy spectrum is shown  
 238 in Figure 6, illustrating that the differential flux of precipitating electron is  $\sim 10^2$  /cm<sup>2</sup>-sr-s-  
 239 keV at 50 keV. The differential electron flux is comparable to that derived from an electron  
 240 density profile measured with the Tromsø EISCAT VHF radar at the same time, assuming  
 241 that an increase of electron density is mainly due to electron precipitation.

242

#### 243 4 Discussion

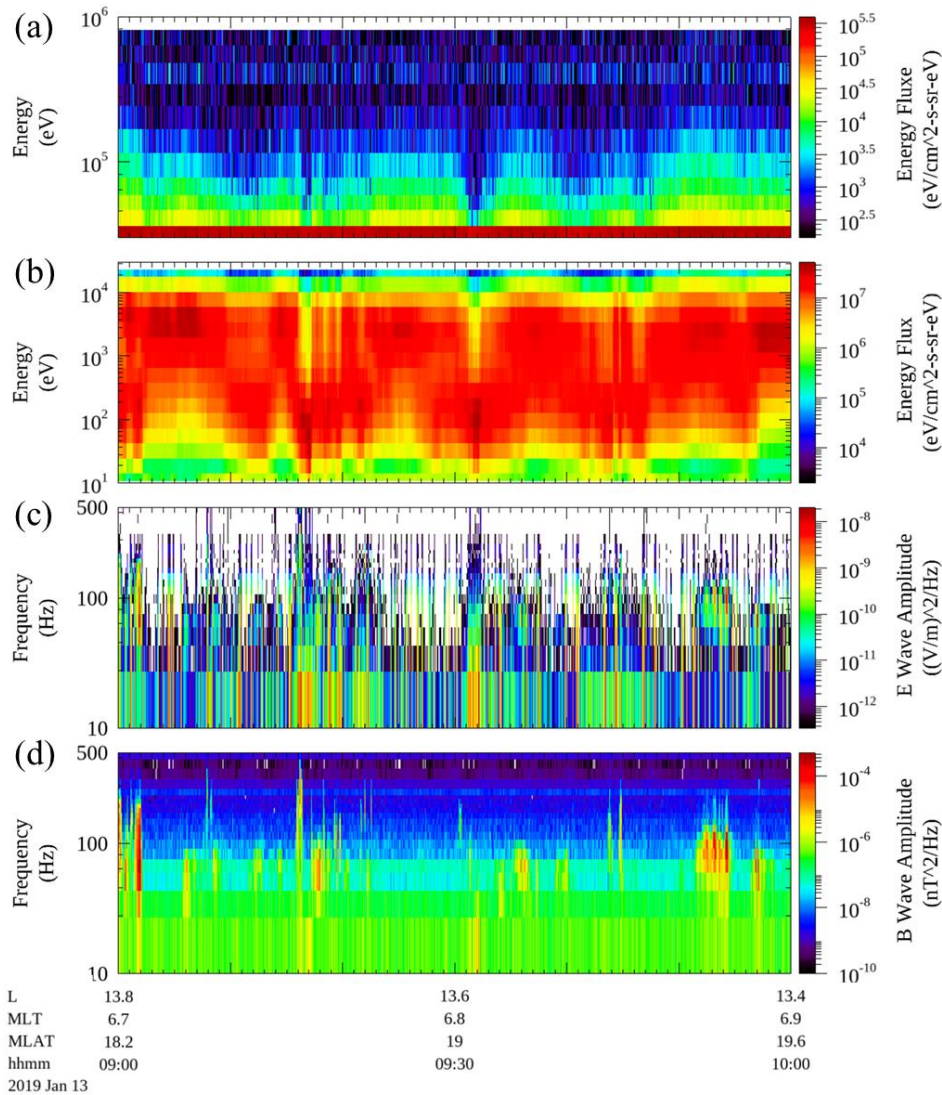
244 We investigated the precipitating electrons on the dayside by using the energetic electron  
 245 detector which can observe energy spectrum of 30–100 keV electrons, and found  
 246 precipitating electrons peaking at  $\sim 50$  keV. Here we discuss whether this electron  
 247 precipitation can be explained by the pitch angle scattering by chorus waves.

248 Figure 7 provides a frequency-time spectrogram, showing the magnetic field emissions  
 249 obtained by the VLF receiver at Lovozero, Kola peninsula in Russia ( $L \sim 5.4$ ,  $LT \sim 11$  h) near  
 250 the rocket trajectory around the time of electron precipitation. The difference in longitude  
 251 was less than  $15^\circ$ . Although this receiver observation is not strictly conjugated with the  
 252 RockSat-XN measurements, it is helpful to infer whistler-mode wave occurrence in the flux  
 253 tube on which RockSat-XN was located. The footprint of Lovozero was traced to the  
 254 magnetic equator along field line using the Tsyganenko T89 model [Tsyganenko 1988] to  
 255 evaluate the condition of cyclotron resonance between electrons and VLF emissions. The  
 256 obtained magnetic field strength is  $\sim 220$  nT near the magnetic equator, corresponding to the  
 257 cyclotron frequency  $f_{ce}$  of 6.2 kHz. Waves were seen at  $\sim 0.2 - 0.8 f_{ce}$  with a band gap at  $\sim$   
 258  $0.5 f_{ce}$ , typical of chorus waves.



260  
 261 Figure 7. (a) Power spectrogram of magnetic field obtained by the VLF receiver at Lovozero  
 262 in Russia between 0900 and 1000 UT on 13 January 2019. Vertical dotted lines show 220 s  
 263 and 270s after the launch of RockSat-XN. The horizontal dotted line shows 3.1 kHz, which is  
 264  $0.5 f_{ce}$  near the magnetic equator of the field line extending from Lovozero. (b) The rocket  
 265 trajectory and positions of the VLF receiver at Lovozero, THEMIS-E footprint and POES  
 266 footprint in geographical coordinate (black dotted lines). Red dotted lines show geomagnetic  
 267 latitude ( $25^\circ$ ,  $35^\circ$ ,  $45^\circ$ ,  $55^\circ$ ,  $65^\circ$ ,  $75^\circ$ ). Two purple points shows POES footprints at 0910 and  
 268 0920 UT. The thick purple line shows POES NOAA-18 footprint between 0910 and 0914  
 269 UT, when electron precipitation events were seen from the data of the Medium Energy  
 270 Proton and Electron Detector (MEPED) on board the POES satellite.

271  
 272 Chorus waves were also observed in the magnetosphere. Figure 8 shows the energy-time  
 273 spectrogram of electrons and frequency-time spectrograms of the wave electric field and  
 274 wave magnetic field, observed by THEMIS-E satellite [Angelopoulos, 2008]. THEMIS-E was  
 275 located near the dawnside magnetopause as can be seen from the intermittent excursions to  
 276 the magnetosheath in Figures 8a and b. Figures 8c and d show electromagnetic waves at  
 277  $0.1 - 0.6 f_{ce}$  in the magnetosphere, where  $f_{ce}$  is  $\sim 360$  Hz at the minimum magnetic field  
 278 strength along the magnetic flux tube on which THEMIS-E was located, especially at 0918,  
 279 0937 and 0954 UT. To combine, ground-based and magnetospheric observations suggest that  
 280 VLF emissions were generated broadly in the dayside magnetosphere during this period.



281

282

283

284

285

286

287

288

289

290

291

292

293

294

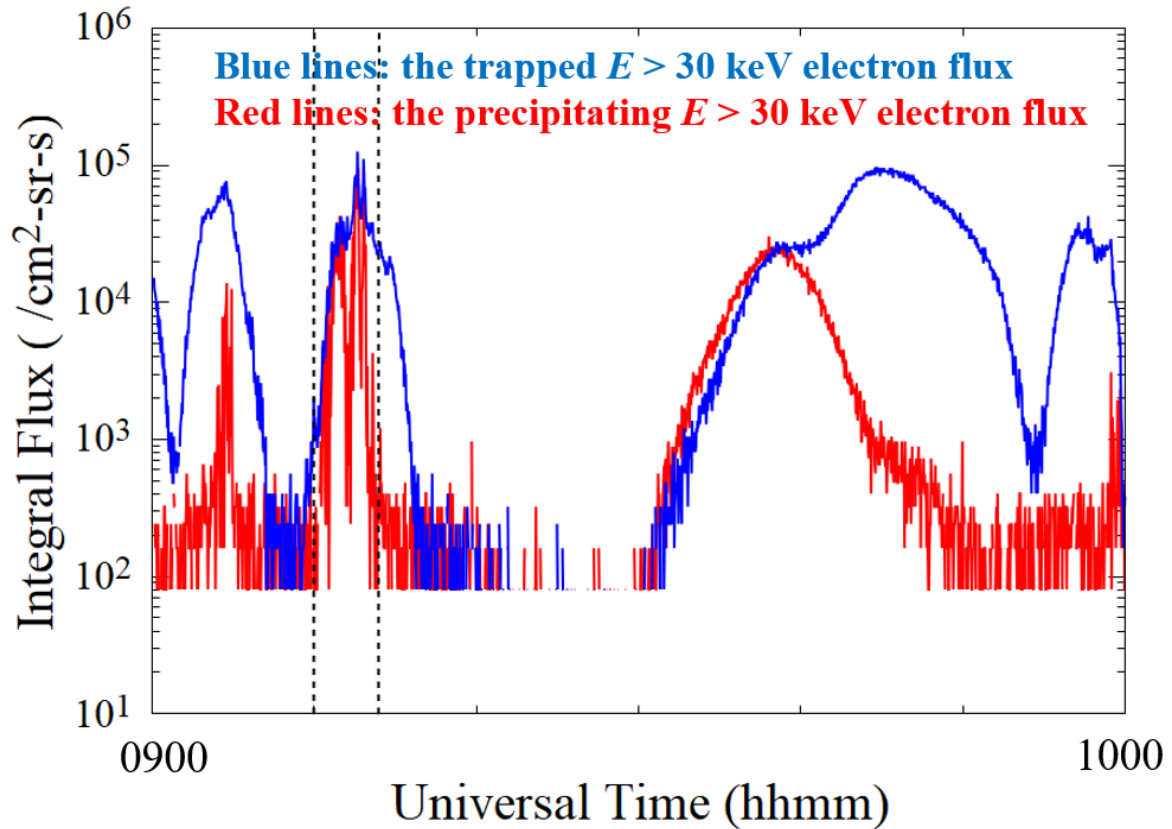
295

296

297

Figure 8. Electron energy-time spectrograms of (a) high energy (from the SST instrument) and (b) low energy (the ESA instrument) components, and frequency-time spectrograms of (c) electric field (from EFI) and (d) magnetic field (SCM), obtained by the THEMIS-E spacecraft during 0900 to 1000 UT on 13 January 2019. THEMIS-E located at  $(X, Y, Z)_{sm} = (4, -12, 3)R_E$  around 0900 UT.

Assuming that observed precipitating  $\sim 50$  keV electrons was scattered at magnetic equator by lower band chorus waves with  $0.1 - 0.5 f_{ce}$ , we can estimate a plasma density by using general resonance condition and the standard cold plasma dispersion relation [e.g. Summers *et al.*, 1998]. We use the magnetic field strength  $\sim 100$  nT at the magnetic equator of the rocket's footprint. The calculated plasma density was  $4 \text{ cm}^{-3}$  and  $0.4 \text{ cm}^{-3}$  assuming chorus waves with  $\sim 0.1 f_{ce}$  and  $0.5 f_{ce}$ , respectively. To compare, the density observed by the THEMIS-E ESA, which was located at higher  $L$  than the rocket trajectory, was  $1 - 2 \text{ cm}^{-3}$ . In addition, the typical plasma density is  $5.6 \pm 1.7 \text{ cm}^{-3}$  at  $L \sim 6.9$  and  $LT \sim 10$  h according to the statistical study by Sheeley *et al.* [2001]. The above calculated plasma density  $4 \text{ cm}^{-3}$  is consistent with these values, thus  $0.1 f_{ce}$  chorus waves is favored for equatorial scattering.



298 Figure 9. The trapped  $E > 30$  keV electron flux (blue lines) and the precipitating  $E > 30$  keV  
 299 electron flux (red lines) measured by MEPED onboard the POES NOAA-18 during 0900 to 1000 UT on 13 January 2019. Vertical dotted lines show 0910 and 0914 UT.  
 300  
 301  
 302

303 The above scenario, the equatorial resonance with  $0.1 f_{ce}$  chorus waves, reasonably explains  
 304 the precipitation of electrons of  $\sim 50$  keV. However, it may contradict with the observed  
 305 energy spectrum peaking at  $\sim 50$  keV. Considering that the flux of 30 keV is typically higher  
 306 than that of 50 keV in the quiet magnetosphere, and lower band chorus waves with  $>0.2 f_{ce}$   
 307 can interact with  $\sim 30$  keV electrons near the magnetic equator for the same condition, the  
 308 precipitation flux peak at  $\sim 50$  keV is not expected. While the apparent peak at  $\sim 50$  keV is  
 309 due to the insufficient statistics (the flux difference was within  $2\sigma$  between 30 and 50 keV),  
 310 here we briefly discuss other possible explanations. One possibility is that the density  
 311 significantly deviates from the typical value. When the density is  $0.1 \text{ cm}^{-3}$ , lower band chorus  
 312 waves with  $0.1 - 0.5 f_{ce}$  can resonate with 50 - 700 keV electrons and not with  $<50$  keV  
 313 electrons. However, such a low density is inconsistent with the observation by THEMIS-E  
 314 and hence we think it is unlikely. Another possible case is that resonance occurred only at the  
 315 high magnetic latitude, where the magnetic field is stronger than the magnetic equator.  
 316 Suppose the chorus waves of  $< 0.5 f_{ce}$  were generated at the equator in the slightly higher L-  
 317 shell region (e.g., the magnetic field intensity  $\sim 70$  nT) and obliquely propagated to the  
 318 magnetic field line of the rocket trajectory, up to the latitude of  $25^\circ$  (the magnetic field  
 319 intensity  $\sim 180$  nT), the 30 keV electrons becomes out of resonance any more [e.g., *Miyoshi*  
 320 *et al.*, 2015b]. In fact, significant wave power of chorus waves with less frequency than a  
 321 typical band gap  $\sim 0.5 f_{ce}$  are frequently observed at magnetic latitudes  $>15^\circ$  on the dayside  
 322 [*Meredith et al.*, 2014]. Therefore, the off-equatorial scattering by obliquely propagating  
 323 chorus waves may be a more plausible scenario than the equatorial scattering, at least for this  
 324 case, in contrast to the statistical view on the nightside [*Kasahara et al.*, 2019].

325 Figure 9 shows the trapped and precipitating electron fluxes (>30 keV) measured by MEPED  
326 onboard the POES NOAA-18 [Evans and Greer, 2000]. The precipitating electron flux was  
327 high during 0910 to 0914 UT, when the trajectory of the POES satellite is shown in the thick  
328 purple line of Figure 7b. This indicates that the precipitation extended to higher L-shell  
329 region, consistent with the chorus emission observed by THEMIS-E. The precipitation was  
330 intermittent, which is also consistent with our observation.

331 Figure 9 shows that the >30 keV integrated flux of precipitating electrons was  $\sim 10^{4.5}$  /cm<sup>2</sup>-sr-  
332 s. Furthermore, statistical surveys on the >30 keV electron precipitation showed that the  
333 integrated flux of precipitating electrons is typically  $\sim 10^4$  /cm<sup>2</sup>-sr-s at  $L > 6$  on the dayside  
334 under quiet geomagnetic condition (AE<100 nT) [Lam et al., 2010]. The precipitation event  
335 observed by MED showed that integrated flux of precipitating electron was  $\sim 10^4$  /cm<sup>2</sup>-sr-s in  
336 30–100 keV, which is lower than observed by POES. This indicates that electron precipitation  
337 was intense at higher latitude where POES was located during 0910 to 0914 UT supporting  
338 the scenario that chorus waves obliquely propagate to inside and scatter the electrons at the  
339 magnetic field line of the rocket trajectory.

340 The duration of the precipitating event was <100 s at RockSat-XN. One of possible causes of  
341 this short period precipitation is the temporal variation of chorus waves. Chorus waves  
342 propagated to Lovozero which have quasi-periodic variations with a timescale  $\sim 50$  s as can  
343 be seen in Figure 7. The intermittent variations of chorus waves may have corresponded to  
344 the transient electron precipitation. Nevertheless, quasi-periodicity  $\sim 50$  s was not found in  
345 electron precipitation at RockSat-XN. We infer that chorus waves may have ceased  
346 temporarily and locally at the rocket's magnetospheric footprint.

## 347 5 Conclusions

348 There have been several observations of chorus waves and precipitating electrons on the  
349 dayside, while their relation has not been verified quantitatively due to the insufficient energy  
350 resolution of conventional low-altitude satellites in the range of 10s-100s keV. Using the  
351 medium-energy electron detector sensitive to 30–100 keV onboard the sounding rocket  
352 RockSat-XN, we confirmed the electron precipitation in the range of typical resonance  
353 energy with chorus waves on the dayside during the geomagnetically quiet periods. Chorus  
354 waves were observed by the ground-based VLF receiver in Lovozero near the launch site and  
355 THEMIS-E spacecraft in the dayside magnetosphere around the period of the precipitation  
356 event. The electron energy is consistent with the resonance energy derived from quasi-linear  
357 theory of magnetospheric electron scattering by chorus waves through cyclotron resonance.  
358 The detailed energy spectrum below 100 keV enabled the discussion suggesting the possible  
359 location of wave-particle interaction.

## 360 Acknowledgments, Samples, and Data

361 We are grateful for the support of NASA Wallops Flight Facility's (WFF) and Andøya Space  
362 Center (ASC). This study was supported by JSPS Bilateral Open Partnership Joint Research  
363 Projects. This study is supported by JSPS Kakenhi (15H05747, 16H06286, 20H01959 and  
364 26707026). The rocket and instruments' data used in this study are available at the UTokyo  
365 Repository (<http://hdl.handle.net/2261/00079366>). The data of VLF receiver used in this  
366 paper are available at the site (<http://aurora.pgia.ru/erg-pgi/case1.html>). Wind data are  
367 available through Coordinated Data Analysis Web (CDAWeb), NASA. The AE index used in  
368 this paper was provided by the WDC for Geomagnetism, Kyoto ([http://wdc.kugi.kyoto-](http://wdc.kugi.kyoto-u.ac.jp/wdc/Sec3.html)  
369 [u.ac.jp/wdc/Sec3.html](http://wdc.kugi.kyoto-u.ac.jp/wdc/Sec3.html)). Science data of the ERG (Arase) satellite were obtained from the  
370 ERG Science Center operated by ISAS/JAXA and ISEE/Nagoya University  
371 (<https://ergsc.isee.nagoya-u.ac.jp/index.shtml.en>; Miyoshi et al, 2018b). The present study

372 analyzed the MEP-e L2-v01\_01 data and orb L2 data obtained by ERG. The present study  
373 used SPEDAS for the data analysis [Angelopoulos *et al.*, 2019]. We acknowledge NASA  
374 contract NAS5-02099 for use of data from the THEMIS mission; specifically, J. W. Bonnell  
375 and F. S. Mozer for use of EFI data, C. W. Carlson and J. P. McFadden for use of ESA data,  
376 A. Roux and O. LeContel for use of SCM data provided under the lead of the Technical  
377 University of Braunschweig and with financial support through the German Ministry for  
378 Economy and Technology and the German Center for Aviation and Space (DLR) under  
379 contract 50 OC 0302. The authors thank the NOAA National Centers for Environmental  
380 Information (NCEI) for providing NOAA POES and documentation  
381 ([https://cdaweb.gsfc.nasa.gov/istp\\_public/data//noaa/noaa18/sem2\\_fluxes-  
382 2sec/2019/noaa18\\_poes-sem2\\_fluxes-2sec\\_20190113\\_v01.cdf](https://cdaweb.gsfc.nasa.gov/istp_public/data//noaa/noaa18/sem2_fluxes-2sec/2019/noaa18_poes-sem2_fluxes-2sec_20190113_v01.cdf)).

383

384

## 385 References

- 386 Anderson, K. A., & Milton, D. W. (1964). Balloon Observations of X Rays in the Auroral  
387 Zone 3. *Journal of Geophysical Research: Space Physics*, 69(21).  
388 <https://doi.org/10.1029/JZ069i021p04457>
- 389 Angelopoulos, V. (2008). The THEMIS mission. *Space Science Reviews* (Vol. 141).  
390 <https://doi.org/10.1007/s11214-008-9336-1>
- 391 Angelopoulos, V., Cruce, P., Drozdov, A., Grimes, E. W., Hatzigeorgiu, N., King, D. A., et  
392 al. (2019). The Space Physics Environment Data Analysis System (SPEDAS). *Space  
393 Science Reviews* (Vol. 215). The Author(s). <https://doi.org/10.1007/s11214-018-0576-4>
- 394 Asikainen, T., & Mursula, K. (2011). Recalibration of the long-term NOAA/MEPED  
395 energetic proton measurements. *Journal of Atmospheric and Solar-Terrestrial Physics*,  
396 73(2–3), 335–347. <https://doi.org/10.1016/j.jastp.2009.12.011>
- 397 Asikainen, T., & Mursula, K. (2013). Correcting the NOAA/MEPED energetic electron  
398 fluxes for detector efficiency and proton contamination. *Journal of Geophysical  
399 Research: Space Physics*, 118(10), 6500–6510. <https://doi.org/10.1002/jgra.50584>
- 400 Blake, J. B., Looper, M. D., Baker, D. N., Nakamura, R., Klecker, B., & Hovestadt, D.  
401 (1996). New high temporal and spatial resolution measurements by SAMPEX of the  
402 precipitation of relativistic electrons. *Advances in Space Research*, 18(8), 171–186.  
403 [https://doi.org/10.1016/0273-1177\(95\)00969-8](https://doi.org/10.1016/0273-1177(95)00969-8)
- 404 Burtis, W. J., & Helliwell, R. A. (1969). Banded Chorus. a New Type of Vlf Radiation  
405 Observed in the Magnetosphere By Ogo 1 and Ogo 3. *Journal of Geophysical Research*.,  
406 74(11), 3002–3010. <https://doi.org/10.1029/ja074i011p03002>
- 407 Evans, D. S., & Greer, M. S. (2000). Polar Orbiting Environmental Satellite Space  
408 Environment Monitor - 2 : Instrument Descriptions and Archive Data Documentation,  
409 Tech. Memo. OAR SEC-93, NOAA, Boulder, Colo.
- 410 Evans, D. S., & Moore, T. E. (1979). Precipitating Electrons Associated With the Diffuse  
411 Aurora: Evidence for Electrons of Atmospheric Origin in the Plasma Sheet. *Journal of  
412 Geophysical Research*, 84(A11), 6451–6457. <https://doi.org/10.1029/JA084iA11p06451>
- 413 Fuller-Rowell, T. J., & Evans, D. S. (1987). Height-integrated Pedersen and Hall conductivity  
414 patterns inferred from the TIROS-NOAA satellite data. *Journal of Geophysical  
415 Research*, 92(A7), 7606. <https://doi.org/10.1029/ja092ia07p07606>
- 416 Han, D., X.-C. Chen, J.-J. Liu, Q. Qiu, K. Keika, Z.-J. Hu, J.-M. Liu, H.-Q. Hu, and H.-G.  
417 Yang (2015), An extensive survey of dayside diffuse aurora based on optical  
418 observations at Yellow River Station, *Journal of Geophysical Research:Space Physics*,  
419 120, 7447–7465, <https://doi.org/10.1002/2015JA021699>

420 Hardy, A., Holeman, E. G., Burke, W. J., Gentile, L. C., & Bounar, K. H. (2008). Probability  
421 distributions of electron precipitation at high magnetic latitudes. *Journal of Geophysical*  
422 *Research: Space Physics*, 113(6), 1–19. <https://doi.org/10.1029/2007JA012746>

423 Hosokawa, K., Miyoshi, Y., Ozaki, M., Oyama, S. I., Ogawa, Y., Kurita, S., et al. (2020).  
424 Multiple time-scale beats in aurora: precise orchestration via magnetospheric chorus  
425 waves. *Scientific Reports*, 10(1), 3380. <https://doi.org/10.1038/s41598-020-59642-8>

426 Kasahara, S., Takashima, T., & Hirahara, M. (2012). Variability of the minimum detectable  
427 energy of an APD as an electron detector. *Nuclear Instruments and Methods in Physics*  
428 *Research, Section A: Accelerators, Spectrometers, Detectors and Associated Equipment*,  
429 664(1), 282–288. <https://doi.org/10.1016/j.nima.2011.11.033>

430 Kasahara, S., Yokota, S., Mitani, T., Asamura, K., Hirahara, M., Shibano, Y., & Takashima,  
431 T. (2018). Medium-energy particle experiments—electron analyzer (MEP-e) for the  
432 exploration of energization and radiation in geospace (ERG) mission. *Earth, Planets and*  
433 *Space*, 70(1), 1–16. <https://doi.org/10.1186/s40623-018-0847-z>

434 Kasahara, S., Miyoshi, Y., Yokota, S., Mitani, T., Kasahara, Y., Matsuda, S., et al. (2018).  
435 Pulsating aurora from electron scattering by chorus waves. *Nature*, 554(7692), 337–340.  
436 <https://doi.org/10.1038/nature25505>

437 Kasahara, S., Miyoshi, Y., Kurita, S., Yokota, S., Keika, K., Hori, T., et al (2019). Strong  
438 diffusion of energetic electrons by equatorial chorus waves in the midnight - to - dawn  
439 sector. *Geophysical Research Letters*, 46. <https://doi.org/10.1029/2019GL085499>

440 Kasahara, S., Takashima, T., Asamura, K., & Mitani, T. (2010). Development of an APD with  
441 large area and thick depletion layer for energetic electron measurements in space. *IEEE*  
442 *Transactions on Nuclear Science*, 57(3 PART 3), 1549–1555.  
443 <https://doi.org/10.1109/TNS.2010.2047752>

444 Keika, K., Spasojevic, M., Li, W., Bortnik, J., Miyoshi, Y., & Angelopoulos, V. (2012).  
445 PENGU In/AGO and THEMIS conjugate observations of whistler mode chorus waves  
446 in the dayside uniform zone under steady solar wind and quiet geomagnetic conditions.  
447 *Journal of Geophysical Research: Space Physics*, 117(7), 1–15.  
448 <https://doi.org/10.1029/2012JA017708>

449 Lam, M. M., Horne, R. B., Meredith, N. P., Glauert, S. A., Moffat-Griffin, T., & Green, J. C.  
450 (2010). Origin of energetic electron precipitation >30 keV into the atmosphere. *Journal*  
451 *of Geophysical Research A: Space Physics*, 115(A4), 1–15.  
452 <https://doi.org/10.1029/2009JA014619>

453 Lampton, M. (1967). Daytime observations of energetic auroral-zone electrons. *Journal of*  
454 *Geophysical Research*, 72(23), 5817–5823. <https://doi.org/10.1029/jz072i023p05817>

455 Li, W., Thorne, R. M., Bortnik, J., Reeves, G. D., Kletzing, C. A., Kurth, W. S., et al. (2013).  
456 An unusual enhancement of low-frequency plasmaspheric hiss in the outer plasmasphere  
457 associated with substorm-injected electrons. *Geophysical Research Letters*, 40(15),  
458 3798–3803. <https://doi.org/10.1002/grl.50787>

459 Li, W., Ni, B., Thorne, R. M., Bortnik, J., Green, J. C., Kletzing, C. A., et al. (2013).  
460 Constructing the global distribution of chorus wave intensity using measurements of  
461 electrons by the POES satellites and waves by the Van Allen Probes. *Geophysical*  
462 *Research Letters*, 40(17), 4526–4532. <https://doi.org/10.1002/grl.50920>

463 Li, W., Ni, B., Thorne, R. M., Bortnik, J., Nishimura, Y., Green, J. C., Kletzing, C. A., Kurth,  
464 G. B., Hospodarsky, H. E., Spence, G. D., Reeves, J. B., Blake, J. F., Fennell, S. G.,  
465 Claudepierre, and X. Gu (2014), Quantifying hiss-driven energetic electron  
466 precipitation: A detailed conjunction event analysis, *Geophys. Res. Lett.*, 41, 1085–1092,  
467 <https://doi.org/10.1002/2013GL059132>

468 Meredith, N. P., Horne, R. B., Sicard-Piet, A., Boscher, D., Yearby, K. H., Li, W., & Thorne,  
469 R. M. (2012). Global model of lower band and upper band chorus from multiple satellite

470 observations. *Journal of Geophysical Research: Space Physics*, 117(10), 1–14.  
471 <https://doi.org/10.1029/2012JA017978>

472 Meredith, N. P., R. B. Horne, W. Li, R. M. Thorne, and A. Sicard-Piet (2014). Global model  
473 of low-frequency chorus ( $f_{LHR} < f < 0.1 f_{ce}$ ) from multiple satellite observations,  
474 *Geophysical Research Letters*, 41, 280–286, <http://doi:10.1002/2013GL059050>.

475 Meredith, N. P., Horne, R. B., Isles, J. D., & Green, J. C. (2016). Extreme energetic electron  
476 fluxes in low Earth orbit: Analysis of POES  $e > 30$ ,  $e > 100$ , and  $e > 300$  keV electrons.  
477 *Space Weather*, 14(2), 136–150. <https://doi.org/10.1002/2015SW001348>

478 Millan, R. M., & Thorne, R. M. (2007). Review of radiation belt relativistic electron losses.  
479 *Journal of Atmospheric and Solar-Terrestrial Physics*, 69(3), 362–377.  
480 <https://doi.org/10.1016/j.jastp.2006.06.019>

481 Miyoshi, Y., Sakaguchi, K., Shiokawa, K., Evans, D., Albert, J., Connors, M., & Jordanova,  
482 V. (2008). Precipitation of radiation belt electrons by EMIC waves, observed from  
483 ground and space. *Geophysical Research Letters*, 35(23), 1–5.  
484 <https://doi.org/10.1029/2008GL035727>

485 Miyoshi, Y., Katoh, Y., Nishiyama, T., Sakanoi, T., Asamura, K., & Hirahara, M. (2010).  
486 Time of flight analysis of pulsating aurora electrons, considering wave-particle  
487 interactions with propagating whistler mode waves. *Journal of Geophysical Research:*  
488 *Space Physics*, 115(10), 1–7. <https://doi.org/10.1029/2009JA015127>

489 Miyoshi, Y., Oyama, S., Saito, S., Kurita, S., Fujiwara, H., Kataoka, R., et al. (2015).  
490 Energetic electron precipitation associated with pulsating aurora: EISCAT and Van  
491 Allen Probe observations. *Journal of Geophysical Research: Space Physics*, 120(4),  
492 2754–2766. <https://doi.org/10.1002/2014JA020690>

493 Miyoshi, Y., Saito, S., Seki, K., Nishiyama, T., Kataoka, R., Asamura, K., et al. (2015).  
494 Relation between fine structure of energy spectra for pulsating aurora electrons and  
495 frequency spectra of whistler mode chorus waves. *Journal of Geophysical Research:*  
496 *Space Physics*, 120(9), 7728–7736. <https://doi.org/10.1002/2015JA021562>

497 Miyoshi, Y., Shinohara, I., Takashima, T., Asamura, K., Higashio, N., Mitani, T., et al.  
498 (2018). Geospace exploration project ERG. *Earth, Planets and Space*, 70(1).  
499 <https://doi.org/10.1186/s40623-018-0862-0>

500 Miyoshi, Y., Hori, T., Shoji, M., Teramoto, M., Chang, T. F., Segawa, T., et al. (2018). The  
501 ERG Science Center. *Earth, Planets and Space*, 70(1). [https://doi.org/10.1186/s40623-](https://doi.org/10.1186/s40623-018-0867-8)  
502 [018-0867-8](https://doi.org/10.1186/s40623-018-0867-8)

503 Newell, P. T., Sotirelis, T., & Wing, S. (2009). Diffuse, monoenergetic, and broadband  
504 aurora: The global precipitation budget. *Journal of Geophysical Research: Space*  
505 *Physics*, 114(9), 1–20. <https://doi.org/10.1029/2009JA014326>

506 Ni, B., Thorne, R. M., Shprits, Y. Y., & Bortnik, J. (2008). Resonant scattering of plasma  
507 sheet electrons by whistler-mode chorus: Contribution to diffuse auroral precipitation.  
508 *Geophysical Research Letters*, 35(11), 1–5. <https://doi.org/10.1029/2008GL034032>

509 Ni, B., Thorne, R. M., Meredith, N. P., Horne, R. B., & Shprits, Y. Y. (2011). Resonant  
510 scattering of plasma sheet electrons leading to diffuse auroral precipitation: 2.  
511 Evaluation for whistler mode chorus waves. *Journal of Geophysical Research: Space*  
512 *Physics*, 116(4), 1–17. <https://doi.org/10.1029/2010JA016233>

513 Ni, B., W. Li, R. M. Thorne, J. Bortnik, J. C. Green, C. A. Kletzing, W. S. Kurth, G. B.  
514 Hospodarsky, and M. de Soria-Santacruz Pich (2014), A novel technique to construct  
515 the global distribution of whistler mode chorus wave intensity using low-altitude POES  
516 electron data, *J. Geophys. Res. Space Physics*, 119, 5685–5699.  
517 <https://doi:10.1002/2014JA019935>

518 Nishimura, Y., Bortnik, J., Li, W., Thorne, R. M., Lyons, L. R., Angelopoulos, V., et al.  
519 (2010). Identifying the driver of pulsating aurora. *Science*, 330(6000), 81–84.  
520 <https://doi.org/10.1126/science.1193186>

521 Nishimura, Y., Bortnik, J., Li, W., Thorne, R. M., Ni, B., Lyons, L. R., et al. (2013).  
522 Structures of dayside whistler-mode waves deduced from conjugate diffuse aurora.  
523 *Journal of Geophysical Research: Space Physics*, 118(2), 664–673.  
524 <https://doi.org/10.1029/2012JA018242>

525 Nishimura, Y., Lessard, M. R., Katoh, Y., Miyoshi, Y., Grono, E., Partamies, N., et al.  
526 (2020). Diffuse and Pulsating Aurora. *Space Science Reviews*, 216(1), 1–38.  
527 <https://doi.org/10.1007/s11214-019-0629-3>

528 Ogasawara, K., Asamura, K., Mukai, T., & Saito, Y. (2005). Avalanche photodiode for  
529 measurement of low-energy electrons. *Nuclear Instruments and Methods in Physics*  
530 *Research, Section A: Accelerators, Spectrometers, Detectors and Associated Equipment*,  
531 545(3), 744–752. <https://doi.org/10.1016/j.nima.2005.02.026>

532 Ogasawara, K., Hirahara, M., Miyake, W., Kasahara, S., Takashima, T., Asamura, K., et al.  
533 (2008). High-resolution detection of 100 keV electrons using avalanche photodiodes.  
534 *Nuclear Instruments and Methods in Physics Research, Section A: Accelerators,*  
535 *Spectrometers, Detectors and Associated Equipment*, 594(1), 50–55.  
536 <https://doi.org/10.1016/j.nima.2008.05.056>

537 Ogasawara, K., Livi, S. A., Allegrini, F., Broiles, T. W., Dayeh, M. A., Desai, M. I., et al.  
538 (2016). Journal of Geophysical Research : Space Physics Next-generation solid-state  
539 detectors for charged Special Section : *Journal of Geophysical Research: Space Physics*,  
540 1–17. <https://doi.org/10.1002/2016JA022559.Abstract>

541 Ogasawara, K., Asamura, K., Takashima, T., Saito, Y., & Mukai, T. (2006). Rocket  
542 observation of energetic electrons in the low-altitude auroral ionosphere during the  
543 DELTA campaign. *Earth, Planets and Space*, 58(9), 1155–1163.  
544 <https://doi.org/10.1186/BF03352005>

545 Ozaki, M., Miyoshi, Y., Shiokawa, K., Hosokawa, K., Oyama, S. ichiro, Kataoka, R., et al.  
546 (2019). Visualization of rapid electron precipitation via chorus element wave–particle  
547 interactions. *Nature Communications*, 10(1). [https://doi.org/10.1038/s41467-018-07996-](https://doi.org/10.1038/s41467-018-07996-z)  
548 [z](https://doi.org/10.1038/s41467-018-07996-z)

549 Parks, G. K. (2013). Microburst Precipitating Phenomena. *Journal of Chemical Information*  
550 *and Modeling*, 53(9), 1689–1699. <https://doi.org/10.1017/CBO9781107415324.004>

551 Santolík, O., Gurnett, D. A., Pickett, J. S., Parrot, M., & Cornilleau-Wehrlin, N. (2003).  
552 Spatio-temporal structure of storm-time chorus. *Journal of Geophysical Research:*  
553 *Space Physics*, 108(A7), 1–14. <https://doi.org/10.1029/2002JA009791>

554 Sazhin, S. S., & Hayakawa, M. (1992). Magnetospheric chorus emissions: A review.  
555 *Planetary and Space Science*, 40(5), 681–697. [https://doi.org/10.1016/0032-](https://doi.org/10.1016/0032-0633(92)90009-D)  
556 [0633\(92\)90009-D](https://doi.org/10.1016/0032-0633(92)90009-D)

557 Sheeley, B. W., Moldwin, M. B., Rassoul, H. K., & Anderson, R. R. (2001). An empirical  
558 plasmasphere and trough density model: CRRES pbservations. *Journal of Geophysical*  
559 *Research: Space Physics*, 106(2000). <https://doi.org/10.1029/2000JA000286>

560 Summers, D., Thorne, R. M., & Xiao, F. (1998). Relativistic theory of wave-particle resonant  
561 diffusion with application to electron acceleration in the magnetosphere. *Journal of*  
562 *Geophysical Research: Space Physics*, 103(A9), 20487–20500.  
563 <https://doi.org/10.1029/98JA01740>

564 Thorne, R. M., Ni, B., Tao, X., Horne, R. B., & Meredith, N. P. (2010). Scattering by chorus  
565 waves as the dominant cause of diffuse auroral precipitation. *Nature*, 467(7318), 943–  
566 946. <https://doi.org/10.1038/nature09467>

567 Thorne, R. M. (1977). Energetic radiation belt electron precipitation: A natural depletion  
568 mechanism for stratospheric ozone. *Science*, 195(4275), 287–289.  
569 <https://doi.org/10.1126/science.195.4275.287>

570 Tsurutani, B. T., & Smith, E. J. (1974). Postmidnight chorus: A substorm phenomenon.  
571 *Journal of Geophysical Research*, 79(1), 118–127.  
572 <https://doi.org/10.1029/ja079i001p00118>

573 Tsurutani, B. T., & Smith, E. J. (1977). Two types of magnetospheric ELF chorus and their  
574 substorm dependences. *Journal of Geophysical Research*, 82(32), 5112–5128.  
575 <https://doi.org/10.1029/ja082i032p05112>

576 Tsurutani, B. T., Verkhoglyadova, O. P., Lakhina, G. S., & Yagitani, S. (2009). Properties of  
577 dayside outer zone chorus during HILDCAA events: Loss of energetic electrons.  
578 *Journal of Geophysical Research: Space Physics*, 114(3), 1–19.  
579 <https://doi.org/10.1029/2008JA013353>

580 Tsyganenko, N. A. (1989). A magnetospheric magnetic field model with a warped tail current  
581 sheet. *Planetary and Space Science*, 37(1), 5–20. [https://doi.org/10.1016/0032-](https://doi.org/10.1016/0032-0633(89)90066-4)  
582 [0633\(89\)90066-4](https://doi.org/10.1016/0032-0633(89)90066-4)

583 Turunen, E., Kero, A., Verronen, P. T., Miyoshi, Y., Oyama, S. I., & Saito, S. (2016).  
584 Mesospheric ozone destruction by high-energy electron precipitation associated with  
585 pulsating aurora. *Journal of Geophysical Research*, 121(19), 11852–11861.  
586 <https://doi.org/10.1002/2016JD025015>

587 Vaivads, A., Santolík, O., Stenber, G., André, M., Owen, C. J., Canu, P., & Dunlop, M.  
588 (2007). Source of whistler emissions at the dayside magnetopause. *Geophysical*  
589 *Research Letters*, 34(9), 1–5. <https://doi.org/10.1029/2006GL029195>

590 World Data Center for Geomagnetism, Kyoto, M. Nose, T. Iyemori, M. Sugiura, T. Kamei  
591 (2015). Geomagnetic AE index. <https://doi:10.17593/15031-54800>

592 Whittaker, I. C., Rodger, C. J., Clilverd, M. A., & Sauvaud, J.-A. (2014). The effects and  
593 correction of the geometric factor for the POES/MEPED electron flux instrument using  
594 a multisatellite comparison. *Journal of Geophysical Research: Space Physics*, 119(8),  
595 6386–6404. <https://doi.org/10.1002/2014ja020021>

596 Yando, K., Millan, R. M., Green, J. C., & Evans, D. S. (2011). A Monte Carlo simulation of  
597 the NOAA POES Medium Energy Proton and Electron Detector instrument. *Journal of*  
598 *Geophysical Research: Space Physics*, 116(10), 1–13.  
599 <https://doi.org/10.1029/2011JA016671>  
600

Figure 1.

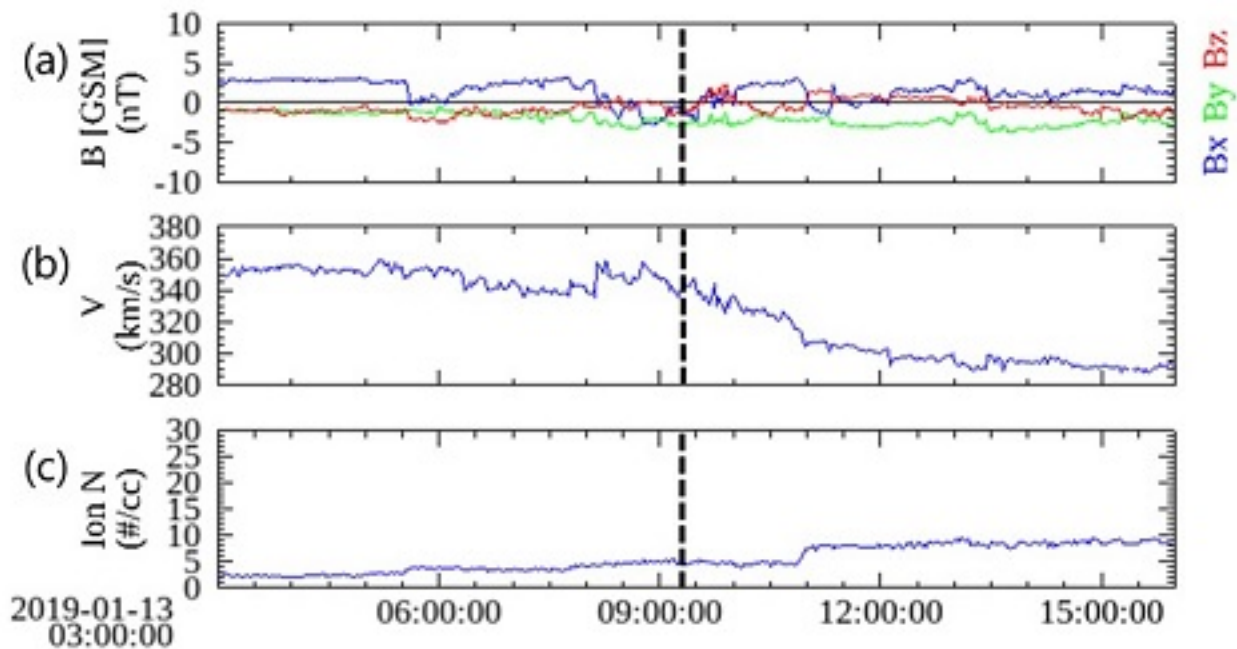
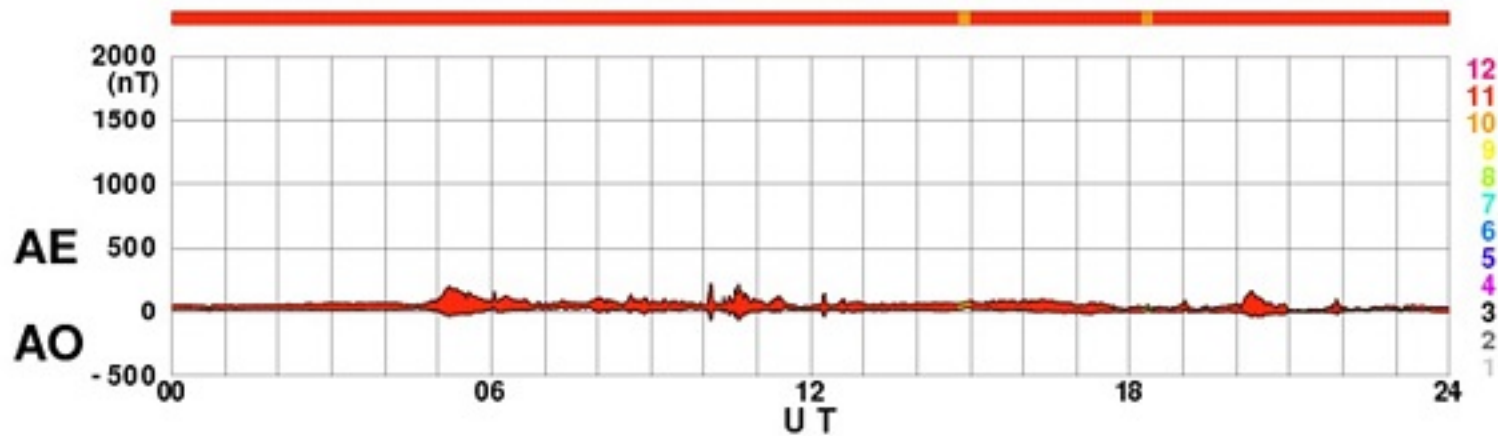


Figure 2.

2019/01/13

AE(11) (Real-Time)

WDC for Geomagnetism, Kyoto



[Created at 2019-04-30 15:14UT]

Figure 3.

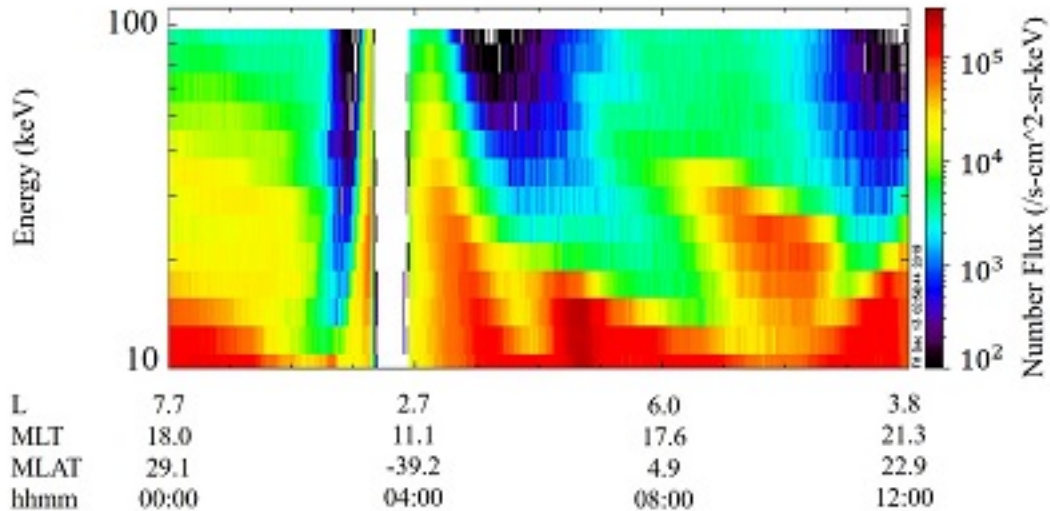


**Figure 4.**

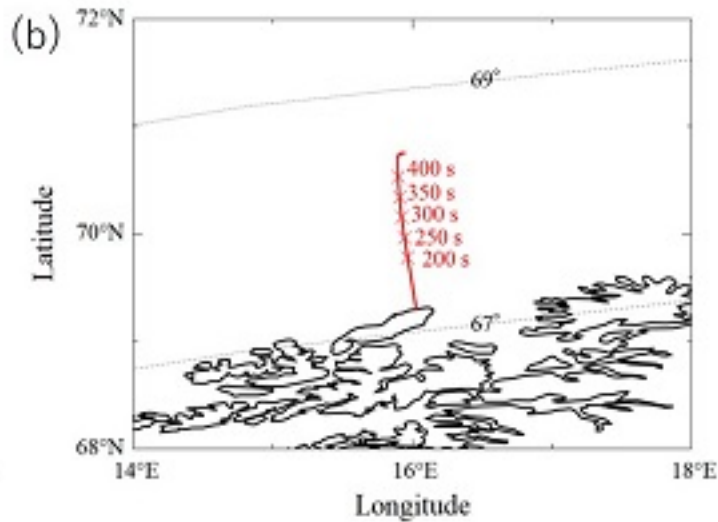
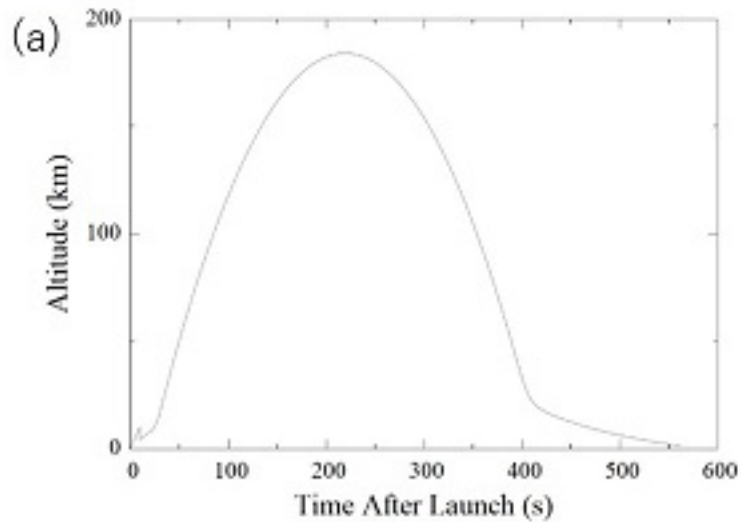
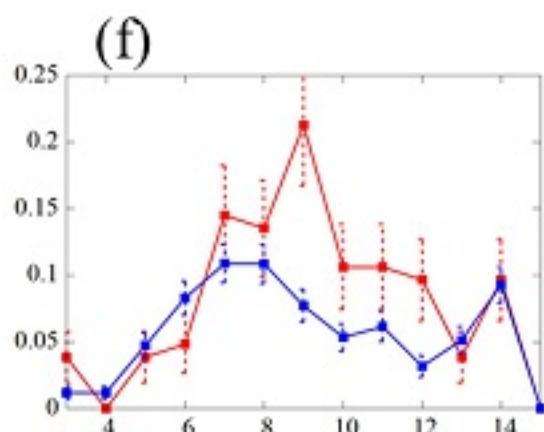
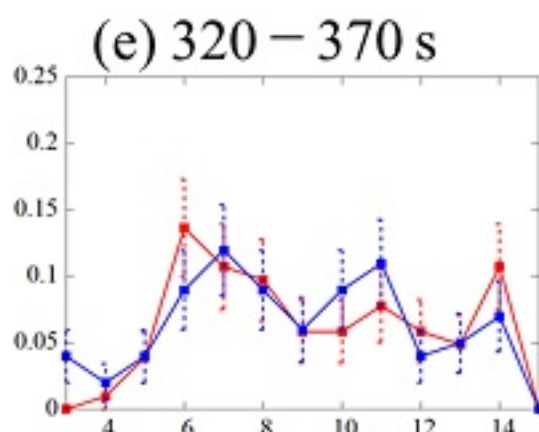
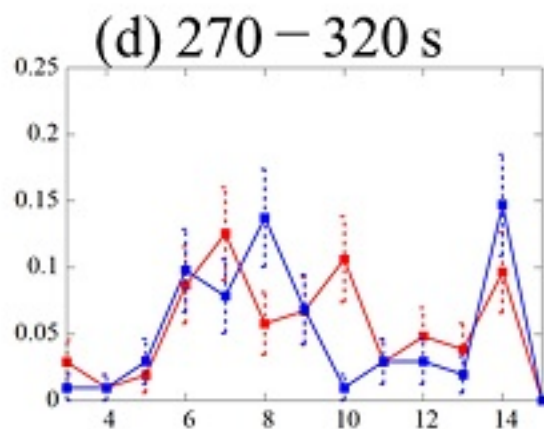
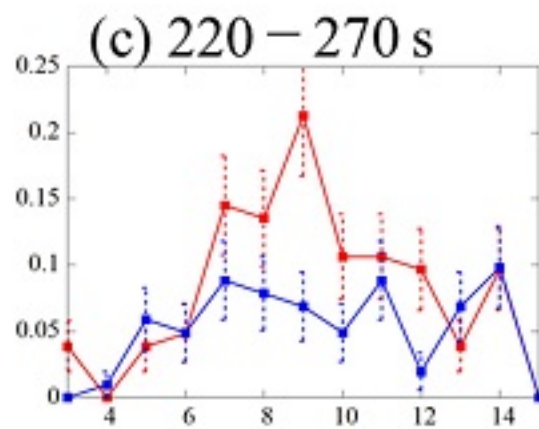
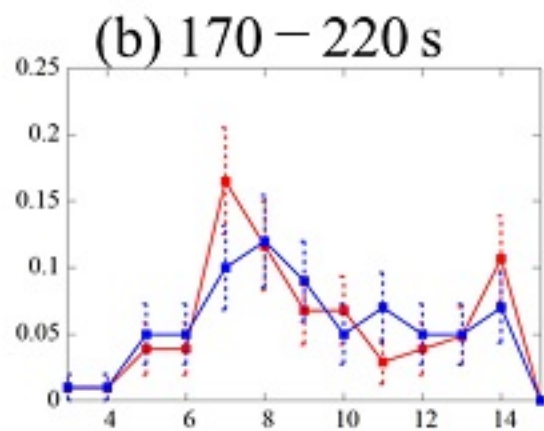
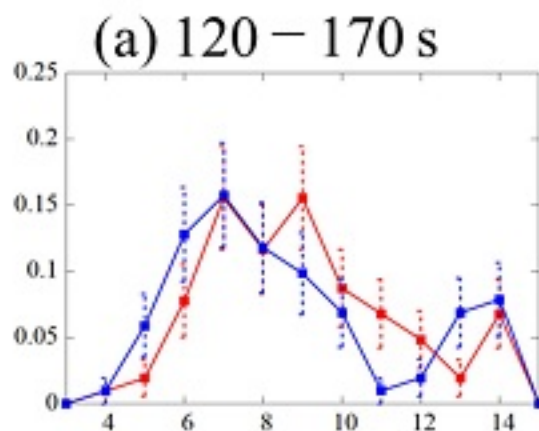


Figure 5.

Count rate (/ s)



Pulse Height Channels

Figure 6.

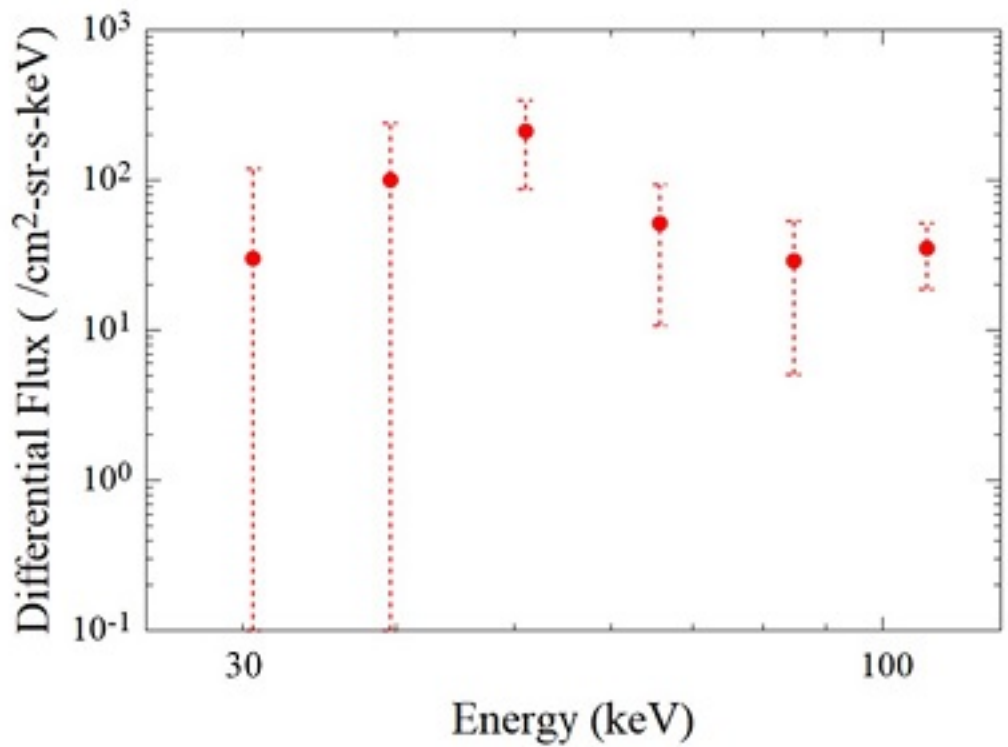


Figure 7.

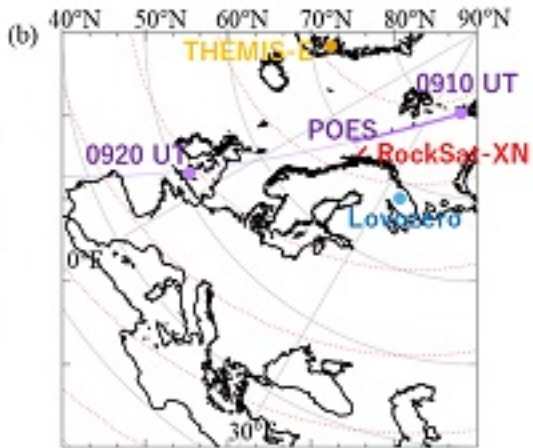
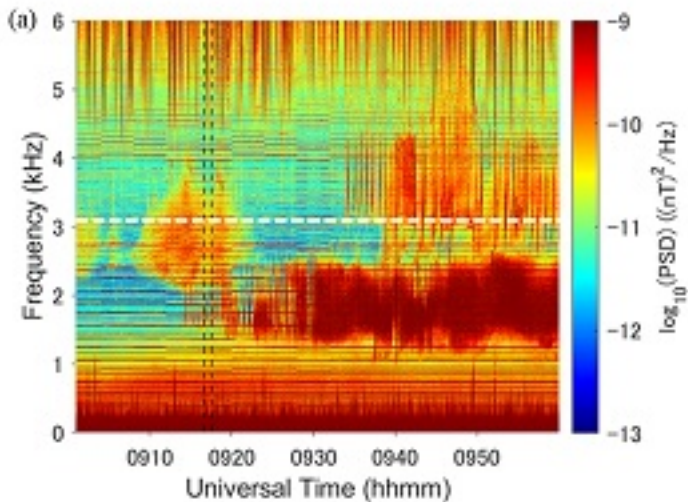
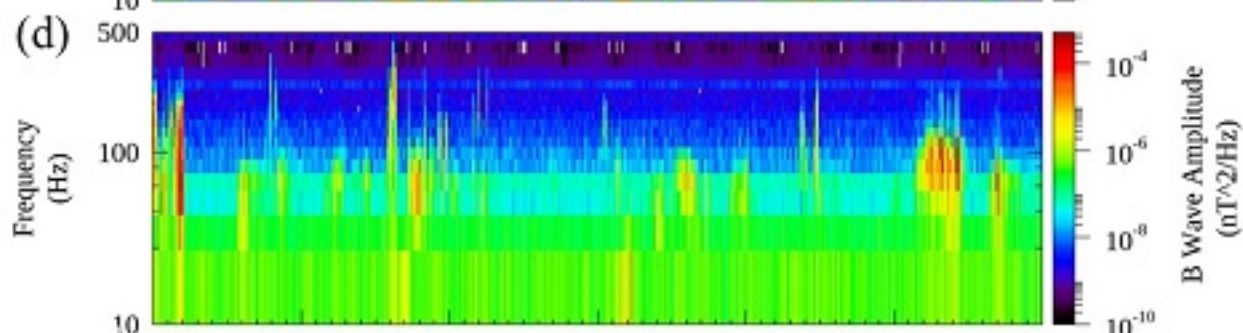
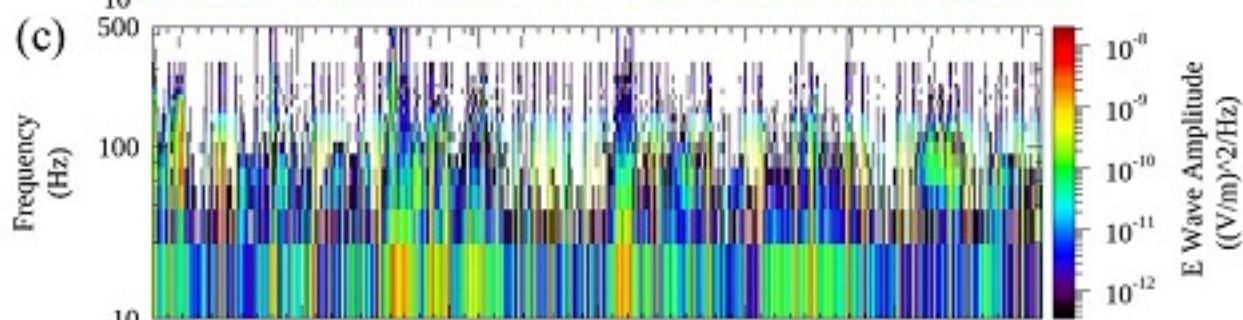
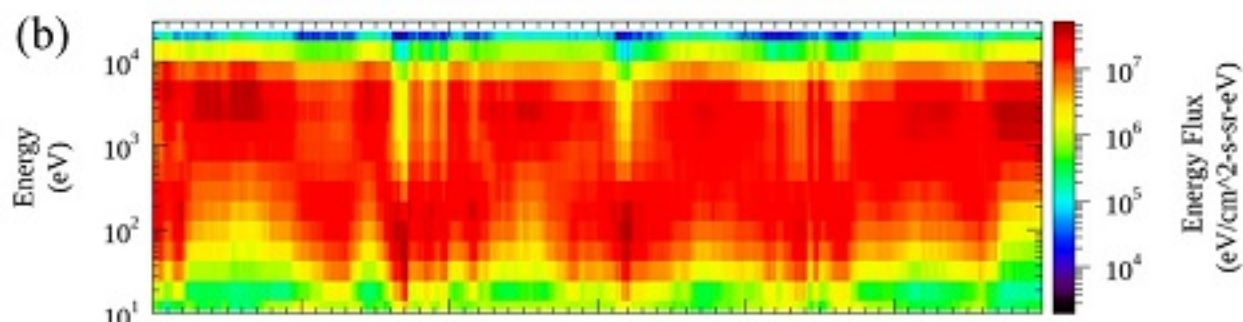
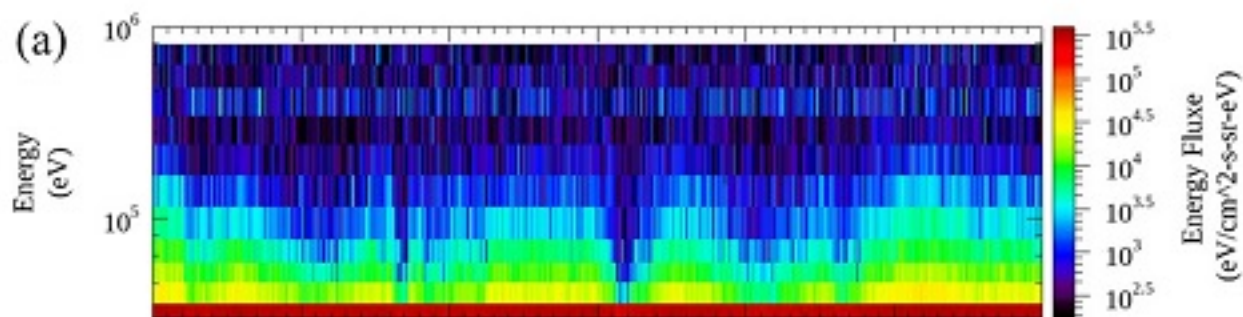


Figure 8.



L	13.8	13.6	13.4
MLT	6.7	6.8	6.9
MLAT	18.2	19	19.6
hhmm	09:00	09:30	10:00

2019 Jan 13

Figure 9.

